Research article

Geoenergy

https://doi.org/10.1144/geoenergy2023-050 | Vol. 2 | 2024 | geoenergy2023-050

One-dimensional modelling of air injection into abandoned oil fields for heat generation

Benjamin M. Storey[1*], Richard H. Worden[1*], David D. McNamara[1], John Wheeler[1], Julian Parker[1,2] and Andre Kristen[2]

[1] Department of Earth, Ocean and Ecological Sciences, School of Environmental Sciences, University of Liverpool, Liverpool L69 3GP, UK
[2] Tayhope, Egerton House, 2 Tower Road, Birkenhead CH4 1FN, UK
BMS, 0000-0003-3213-3134; RHW, 0000-0002-4686-9428; DDMcN, 0000-0001-9789-2436; JW, 0000-0002-7576-4465
*Correspondence: BMS, benjamin.storey@liverpool.ac.uk; RHW, rworden@liverpool.ac.uk

Abstract: With the global drive for net-zero emissions, it has never been more important to find clean energy sources. There are thousands of abandoned oilfields worldwide with the potential to be reactivated to produce clean energy with air injection and subsequent waste fluid sequestration. Air injection, and the development of a fire-front, may be used with enhanced geothermal systems by taking advantage of the inherent increase in heat and pressure. Conventionally used as an enhanced oil recovery technique, air injection has gained the reputation of being a high-risk intervention due to the many failures in its history. Knowledge of how petrophysical rock properties and oil physical and chemical properties control the consequences of air injection is key to optimzing the selection of late-life, or even abandoned oilfields for use in such systems. Here we use one-dimensional modelling to test the effect of varying porosity, permeability, oil viscosity and API gravity on the success of air injection. Modelling shows that the most important factor controlling temperature is the porosity of the reservoir, followed by the API gravity and then the viscosity of the oil. The most important factors controlling velocity of the fire-front are API gravity followed by oil viscosity. We show that reservoirs with high porosity and low permeability with high viscosity and low API gravity oil reach the highest fire-front temperatures. The significance of this work is that it provides several geoscience-related criteria to rank possible candidate reservoirs for reactivation and clean energy generation via air injection: the best candidates will have the highest total porosity, relatively low permeability, highest oil viscosity and lowest API gravity, such fields can then move on to bespoke and more complex simulations.

Received 22 November 2023; **revised** 12 March 2024; **accepted** 12 March 2024

Considering the UK government's target of net-zero carbon emissions by 2050 (Department for Business 2020), the need to find clean sources of energy has never been more important. Use of enhanced geothermal systems (EGS) is a promising technique with which zero-carbon energy can be produced. Globally, there are tens of thousands of oilfields that have produced hydrocarbons, that are no longer economically viable. Oil fields typically have maximum recovery factors of about 30 to 35% (Shepherd 2009) and therefore still contain considerable oil resources (i.e. up to 65 to 70% of the original oil volume) when they become non-economic by conventional primary or secondary (pressure support) production methods (Shepherd 2009; Cinar 2013). These depleted oil fields may be adapted to produce clean energy via the use of air injection, via the exploitation of the inherent increase in heat and pressure through thermogenically-induced geothermal means. Oxidation of oil is an exothermic process that releases large quantities of heat, in this case, within the reservoir. This heat may be exploited by the use of a geothermal heat exchanger (Cinar 2013; Li *et al.* 2014; Templeton *et al.* 2014; Zhu *et al.* 2019). The enthalpy generated by the increased temperature within the reservoir can create an artificial geothermal system, which could be exploited in the same manner as a conventional or enhanced geothermal system (Zhu *et al.* 2019).

To meet the criteria of clean energy, the energy must be produced with no emissions into the atmosphere; this can be achieved by the sequestration of produced fluids (e.g. hydrocarbons, carbon monoxide, carbon dioxide, etc.) immediately from the production well in a closed loop system, with the energy generated purely from enthalpy generation in enhanced geothermal systems and the thermogenic process and not used as conventional enhanced oil recovery (EOR) (Aikman 2022; Storey *et al.* 2022).

The ability to repurpose infrastructure used for the original oil field production would potentially reduce project setup costs by eliminating the costs associated with new well drilling in conventional geothermal methods. Repurposing wells might also reduce the environmental footprint by minimizing the release of environmentally damaging gases leaking from improperly abandoned wells (Schiffner *et al.* 2021).

Background of air injection

Air injection, also referred to as *in situ* combustion (ISC), has primarily been used as a thermal enhanced oil recovery technique (Ren *et al.* 2002). Air injection and ISC have been used with relatively low degrees of success since the 1920s (Wu and Fulton 1971; Burger 1972; Turta *et al.* 2007; Speight 2019). Air injection has generally been considered to be a high risk process given that around 55% of projects undertaken in the USA between 1960 and 1998 were deemed to be a failure (Sarathi 1999; Storey *et al.* 2022). Such failures have been retrospectively attributed to poor selection of opportunities based on reservoir choice and poor project design. For example, the Hospah Field, New Mexico, USA, was not appropriate for air injection. A low permeability coal seam within the Hospah reservoir unit caused the injected air to preferentially migrate through the upper water and transition zones, where there was low oil saturation, and away from the zones of high oil saturation (Struna and Poettmann 1988).

During air injection, a portion of the oil in the reservoir is ignited and the subterranean fire is subsequently propagated across the reservoir as a high temperature fire-front, fed by oxygen in the injected air. Ahead of the fire-front, there are several zones including the coking zone, the cracking zone, the steam plateau, the water bank, and the oil bank (Fig. 1) (Wu and Fulton 1971). The coking zone provides fuel (coke) for the advancing fire-front, which burns, in the presence of oxygen, at temperatures greater than 350°C. The flue gases in the cracking zone and the steam plateau drive the liquids in the water bank and oil bank ahead of them towards the production well. During this series of processes, there are different sets of oxidation reactions that occur; low temperature oxidation reactions, below 300°C (LTO); medium temperature oxidation reactions, also known as fuel deposition reactions, between 300 and 350°C (MTO) and high temperature oxidation reactions, above 350°C (HTO) (Storey *et al.* 2022).

While there is much research on ISC, some field-scale simulation studies use from around 4000 to over 10 000 mD permeability and around 30 to 36% porosity as standard (Ito and Chow 1988; Bottia-Ramirez *et al.* 2017; Yang *et al.* 2019; Zhu *et al.* 2021; Ado 2022; Ji *et al.* 2022), this is not generally representative of what is seen in the North Sea Basin or most other sedimentary basins. Good quality reservoirs may typically have between 20 and 30% porosity, such as the Captain Field (Hodgins *et al.* 2020), but it is not uncommon for reservoirs to be outside of this range (Gluyas and Swarbrick 2004). Examples of such reservoirs from the North Sea range from 9% average porosity in the Buchan Field (Wynn and Saundry 2020), up to 30% average porosity in the Forties Field (Rose *et al.* 2020). Permeability varies by orders of magnitude between fields, such as the Eldfisk Field (2 mD) (Cook and Brekke 2004) and the Piper Field (4000 mD) (Harker 1998). Many fields contain orders of magnitude variations of permeability within the same reservoir unit, such as the Forties Field (ranging from 10 to 2000 mD) (Rose *et al.* 2020) and the Fife Field (0.01 to 5500 mD) (Mackertich 1996). For reservoirs to have permeability up to 10 000 mD is uncommon, but this is found in parts of the Kraken and Mariner fields, for example (Parkes *et al.* 2020; Silcock *et al.* 2020).

Careful consideration and integration of lessons from field applications, experimental studies and numerical modelling should help to mitigate failure of future air injection projects (Storey *et al.* 2022), and thus lead to more examples of highly successful and long-running air-injection projects such as the one at Bellevue Oil Field, Louisiana, USA, which has been running for over 50 years (Joseph *et al.* 1983; Turta *et al.* 2007; Sharma *et al.* 2021). Despite the various successes and many failures, there has been relatively little research into the geological and petrophysical controls on the efficacy of air injection. While it has been stated that laboratory testing, followed by modelling, is the optimum design cycle (Gutierrez *et al.* 2009), each reservoir has a unique combination of petrophysical and oil physical properties. This present study aims to address the complex interaction of petrophysical and oil property effects, using one-dimensional numerical modelling as a pre-selection step (Fig. 2) to assess how geological (petrophysical) and oil physical properties affect the process and address the following questions:

(1) What is the effect of varying petrophysical rock properties on the temperature and velocity of the fire front?
(2) What is the effect of varying oil physical properties on the temperature and velocity of the fire front?
(3) What are the interdependencies of the various petrophysical and oil physical properties, and which of these properties predominantly control the temperature and velocity of the fire-front during the ISC process?
(4) How do the controls on temperature and velocity affect the enthalpy rate and arrival time of the fire-front at the producer well?

Methodology

This study uses one-dimensional reservoir modelling, to create simple and fast models to explore the effect of multiple different parameters on air injection. These models have been created in the commercial simulator, STARS, a three-phase multi component thermal and steam additive simulator, developed by the Computer Modelling Group. The simulator consists of one conservation equation for each component, as well as equations describing phase equilibrium for each grid block and an equation describing the operating conditions of each injector and producer well (CMG 2020).

A one-dimensional Cartesian grid was constructed to represent the reservoir between the injection and production wells. The effect of heat loss to the under- and over-burden has been included in these models, making the models not truly one-dimensional; this produces a more realistic representation of temperatures that may be observed at field scale. The heat loss into the over- and under-burden is modelled by simulator-defaults set out by STARS (Vinsome and Westerveld 1980; CMG 2020). The initial temperature of the over- and under-burden are assumed to be the same as the reservoir. Heat loss into the laterally adjacent reservoir is not modelled in this study as it is not intended to resemble the entire areal extent of a reservoir horizon. The grid was populated with basic rock properties (Table 1), a fluid model (Table 2), and a one-dimensional simulation model with varying petrophysical properties (Table 3).

Grid size sensitivity analysis

In reality a fire-front has been reported to be only several centimetres thick (Sarathi 1999; Zhu 2011; Zhu *et al.* 2021); in theory a model should reproduce this very narrow fire-front, but cm-scale grid-blocks have not here been used due to simulation time-constraints associated with field scale models (Zhu 2011). To test the effect of grid block size on the temperature and relative

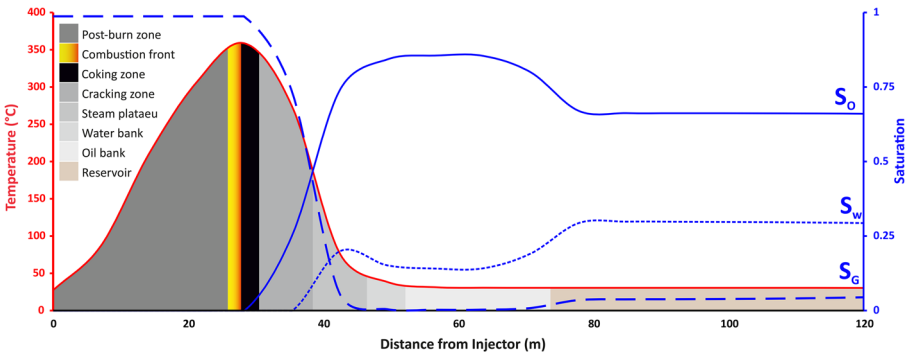

Fig. 1. Schematic diagram showing a numerically modelled graph showing the water, oil, and gas saturation along with the temperature profiles in the different zones created between the injector and producer during dry forward *in situ* combustion.

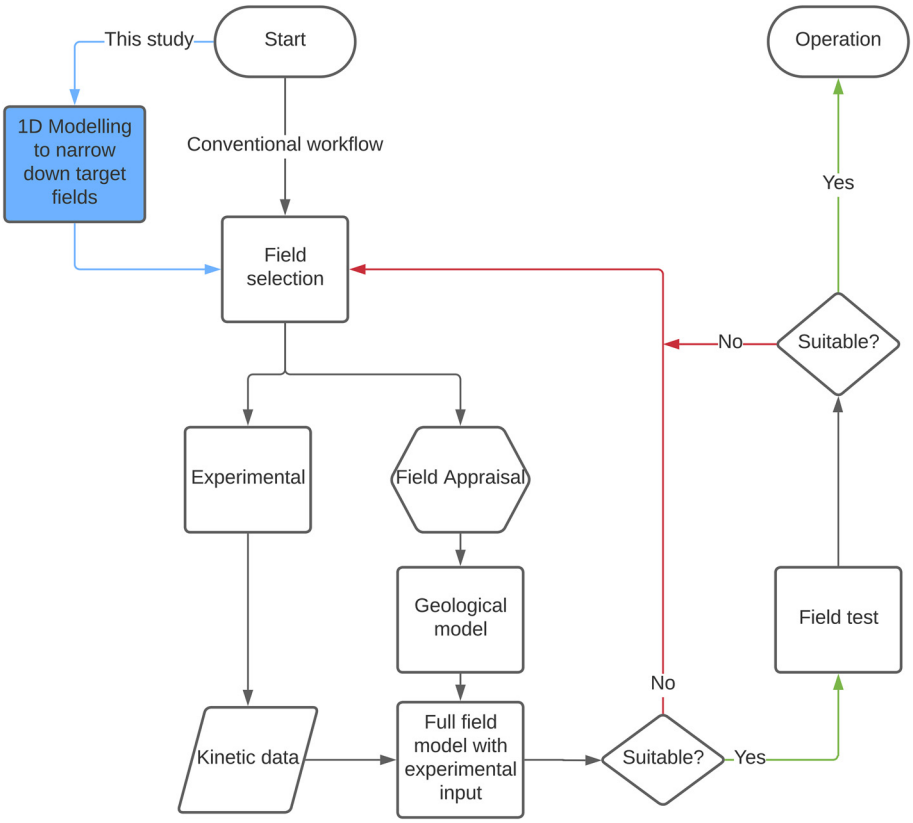

Fig. 2. Work flow diagram to show where this method of modelling can be used with the conventional work flow to help to narrow down potential targets for this process.

position of the fire-front, several grid block sizes have been tested while retaining the same overall reservoir dimensions. Grid block size affects the temperature and relative position of the fire-front due to the effect of fuel volume per grid block; larger grid blocks contain more fuel and therefore take longer to burn before moving on to the next cell, thus resulting in higher temperatures and a slower moving fire-front (Zhu 2011). Our grid size sensitivity analysis has shown that the grid size effect on temperature is negligible between 200 and 1000 grid blocks (Fig. 3). With the time difference to perform one model at 200 and one at 500 grid blocks increasing four-fold, and 12-fold for 1000 (Table 4), we have utilized 200 grid blocks as an appropriate representation of the temperature and velocity of the fire-front, with an error of $\pm 4\ \mathrm{m\ yr^{-1}}$ for velocity because the relative change between models will be unaffected (Fig. 3).

Fluid and reaction model

All models inject the same volume of air over the duration of the simulation. Eight fluid models have been used in this study. Fluid models from Alba, Captain, Clair, Kraken and Mariner (Table 2) have been derived from density and initial viscosity data from specific North Sea oil fields (Hodgins *et al.* 2020; Moore *et al.* 2020; Parkes *et al.* 2020; Robertson *et al.* 2020; Silcock *et al.* 2020). Model oils X, Y and Z (Table 2) are simplified conceptual oils with varying density and initial oil viscosity; although these are not based on real oil-field data they are intended to decouple the effects of API gravity and initial oil viscosity, as the API gravity and viscosity are related in the example North Sea oils, this is not always the case, as specific oil chemistry may alter the viscosity of the oil without changing the API gravity and vice versa (Watson *et al.* 1935). Pressure, volume and temperature (PVT) characteristics of all eight oils have been derived using published correlations which are based on a combination of laboratory data and regression analysis (Standing 1947; Ng and Egbogah 1983) (Fig. 4). Gas-liquid 'equilibrium' K-values and critical properties (Table 2) for the

Table 1. Initial conditions and reservoir properties used for all simulations

Reservoir properties and initial conditions	Value
Reservoir property	
Initial reservoir temperature (°C)	38
Initial reservoir pressure (kPa)	10 000
Oil saturation	0.5
Water saturation	0.5
Reservoir geometry	
Dimensions *I*, *j*, *k* (m)	100 × 10 × 10
Dimensions *I*, *j*, *k* (grid blocks)	200 × 1 × 1
Depth (m)	1000
Rock and fluid thermal properties	
Formation compressibility ($\mathrm{kPa^{-1}}$)	1.80×10^{-05}
Volumetric heat capacity ($\mathrm{J\ m^{-3}{\cdot}°C}$)	$2.35 \times 10^{+06}$
Thermal conductivity phase mixing reservoir rock ($\mathrm{J\ m^{-3}{\cdot}°C}$)	$1.50 \times 10^{+05}$
Oil phase heat capacity ($\mathrm{J\ m^{-3}{\cdot}°C}$)	$1.15 \times 10^{+05}$
Water phase heat capacity ($\mathrm{J\ m^{-3}{\cdot}°C}$)	$5.45 \times 10^{+04}$
Gas phase heat capacity ($\mathrm{J\ m^{-3}{\cdot}°C}$)	4000
Volumetric heat capacity – overburden ($\mathrm{J\ m^{-1}{\cdot}day{\cdot}°C}$)	$2.35 \times 10^{+06}$
Volumetric heat capacity – underburden ($\mathrm{J\ m^{-1}{\cdot}day{\cdot}°C}$)	$2.35 \times 10^{+06}$
Thermal conductivity – overburden ($\mathrm{J\ m^{-1}{\cdot}day{\cdot}°C}$)	$1.50 \times 10^{+05}$
Thermal conductivity – underburden ($\mathrm{J\ m^{-1}{\cdot}day{\cdot}°C}$)	$1.50 \times 10^{+05}$
Well constraints	
Injector well constraints – BHP Max (kPa)	30 000
Injector well constraints – surface gas rate Max ($\mathrm{m^3\ day^{-1}}$)	1500
Producer well constraints – BHP Min (kPa)	9800
Injected fluid	
Injected fluid – inert gas (mole fraction)	0.79
Injected fluid – oxygen (mole fraction)	0.21
Injected fluid – temperature (°C)	15
Injected fluid – pressure (kPa)	12 000

Table 2. Kinetic properties for all components used in the reaction scheme, with fluid models Alba, Captain, Clair and Kraken and conceptual oils X, Y and Z

Component		MW kg mol^{-1}	C atoms	P_c kPa	T_c °C	KV1 kPa	KV4 °C	KV5 °C	ρ kg m^{-3}	API Gravity °API	β kPa^{-1}	α °C^{-1}	μ @ 38°C cP
Heavy oil	**Alba**	0.288	18	1317.000	459.850	1.38×10^6	−4294.55	−149.150	892.227	19	1.06×10^{-06}	2.96×10^{-03}	22.271
	Captain	0.293	18	1206.000	471.850	1.34×10^6	−4361.79	−143.250	895.063	19	1.05×10^{-06}	2.96×10^{-03}	404.290
	Clair	0.244	15	1520.000	433.850	1.41×10^6	−4121.51	−161.350	857.576	24	1.22×10^{-06}	2.96×10^{-03}	80.961
	Kraken	0.366	22	853.140	508.804	1.73×10^6	−5214.26	−114.468	943.359	12	8.46×10^{-07}	2.96×10^{-03}	704.170
	Mariner	0.355	22	853.140	508.804	1.73×10^6	−5214.26	−114.468	928.385	14	9.08×10^{-07}	2.96×10^{-03}	2118.810
	Oil X	0.423	26	572.656	543.234	1.91×10^6	−5871.78	−86.844	958.661	10	7.83×10^{-07}	2.96×10^{-03}	46.647
	Oil Y	0.278	17	1317.000	459.850	1.38×10^6	−4294.55	−149.150	885.183	20	1.09×10^{-06}	2.96×10^{-03}	3399.860
	Oil Z	0.423	26	572.656	543.234	1.91×10^6	−5871.78	−86.844	958.661	10	7.83×10^{-07}	2.96×10^{-03}	4664.680
Light oil		0.027	-	2710.000	318.500	4.89×10^6	−4655.90	−273.150	742.000	-	1.00×10^{-06}	9.00×10^{-04}	40.084
H_2O		0.018	-	-	-	-	-	-	994.917	-	4.43×10^{-07}	3.79×10^{-04}	0.767
CO_2		0.028	-	7376.430	31.050	5.32×10^6	−2002.11	−273.150	500.000	-	5.98×10^{-06}	2.96×10^{-03}	0.055
O_2		0.032	-	5046.000	−118.550	5.32×10^6	-	-	-	-	-	-	-
Non-condensable gas (NCG)		0.028	-	3394.390	−146.950	9.07×10^5	−705.20	−273.150	318.000	-	6.00×10^{-06}	3.00×10^{-05}	1.712
Coke		0.012	-	-	-	-	-	-	917.000	-	-	-	-

Table 3. Models that will be used to test different porosity and permeabilities on the propagation of the fire-front, models 1 to 5 vary porosity with a fixed permeability, models 6 to 10 vary permeability with a fixed porosity, and models 11 to 15 vary porosity and permeability with a Carman–Kozeny relationship (equation 5)

Model	Porosity (%)	Permeability (mD)
1	10	1000
2	15	1000
3	20	1000
4	25	1000
5	30	1000
6	15	1
7	15	10
8	15	100
9	15	1000
10	15	10 000
11	10	278
12	15	1052
13	20	2815
14	25	6255
15	30	12 407

component 'heavy oil' have been taken from the STARS manual for components up to C_{20} (Reid *et al.* 1977; CMG 2020) and extrapolations have been used for those above C_{20} (Ambastha and Kumar 1999), number of carbon atoms in each oil model have been calculated from the balanced equations and varies with the API gravity of each oil (Table 2).

For the relative permeability of fluids in the rock, typical curves from water-wet systems have been used for the oil – water and gas – liquid relative permeability curves, with temperature-dependence included (Esmaeili *et al.* 2019) (Fig. 5). As few clastic reservoirs are oil wet, the majority of reservoirs may have mixed wettability (Gluyas and Swarbrick 2004), fractional wettability, or even change wettability following secondary production methods such as water or steam injection (Anderson 1986, 1987), which is a strong possibility in depleted fields. As well as this, wettability varies greatly depending on the oil within the reservoir and the mineralogy of the reservoir rock (Gluyas and Swarbrick 2004), and so more specific and realistic curves are not required at this stage.

A relatively simple reaction model has been employed, based on Crookston's model (Crookston *et al.* 1979) (equations 1–4) because the primary focus of this study is determining the controlling geological and petrophysical properties of the reservoir on the fire-front. Crookston's approach represents the most commonly used reaction model (Jia *et al.* 2016). It has been shown that reaction models with relatively few components and reactions perform better than more complicated schemes with a larger number of components and reactions, particularly when upscaled (Anderson and Kovscek 2022*a*, *b*).

The components used in this reaction scheme are oxygen, non-condensable gas (NCG: in this case nitrogen or carbon monoxide), carbon dioxide, water, coke, a heavy hydrocarbon pseudo-component (provided by the fluid model, in this case) and a light hydrocarbon pseudo-component (which represents a lighter fraction of the fluid model, formed from cracking); properties of the components are listed (Table 5).

The four reactions that have been modelled are:

$$\text{heavy oil} \rightarrow a_1\text{light oil} + xb_1\text{coke} \quad (1)$$

$$\text{heavy oil} + w_2O_2 \rightarrow x_2CO_2 + y_2H_2O + z_2\text{NCG} \quad (2)$$

$$\text{light oil} + w_2O_2 \rightarrow x_3CO_2 + y_3H_2O + z_3\text{NCG} \quad (3)$$

$$\text{coke} + w_4O_2 \rightarrow x_4CO_2 + y_4H_2O + z_4\text{NCG} \quad (4)$$

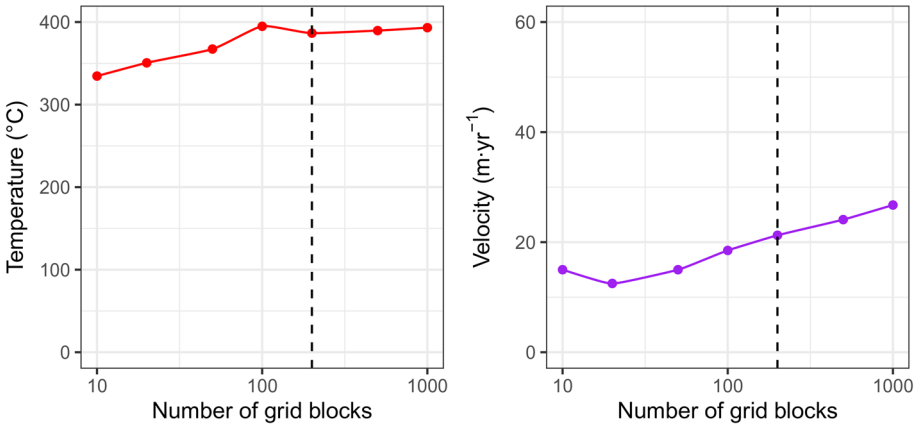

Fig. 3. Grid sensitivity analysis to show how varying the number of grid blocks influences the temperatures and velocities observed during one-dimensional *in situ* combustion models.

The stochiometry of equations (1) and (2) vary depending on the fluid model, dictated by the API gravity of the oil (Table 5), whereas equations (3) and (4) are always the same.

Geological model

In the following simulations, three approaches have been taken in order to assess the specific effects of reservoir quality on air-injection; porosity has been varied for fixed permeability, permeability has been varied for fixed porosity, and porosity and permeability have been allowed to co-vary (Table 3). Hence, geological models 1 to 5 have fixed permeability (1000 mD) with variable porosity (10 to 30%). Models 6 to 10 have fixed porosity (15%) with variable permeability (1 to 10 000 mD). Models 11 to 15 co-vary permeability and porosity using a simplified Carman–Kozeny relationship (equation 5) (Kozeny 1927; Carman 1997). In the Carman–Kozeny relationship, k is permeability (m^2), φ is porosity (fraction) and D is grain diameter (m). In this case grain diameter was set to 200 μm, i.e. upper fine to medium grain size, as many sandstone reservoirs are fine to medium grained (Bjørlykke 2015):

$$k = \frac{\varphi^3 \cdot D^2}{180 \cdot (1-\varphi)^2} \quad (5)$$

The three approaches have been used because the relationship between porosity and permeability is not simple; it can be affected by grain shape, grain size, grain sorting, cementation, clay mineralogy and diagenetic history, it is therefore different for every rock and its specific depositional and diagenetic history (Olivarius *et al.* 2015; Worden and Utley 2022).

The behaviour of each of the eight fluid types (Table 2) was simulated in CMG STARS using each of the 15 geological models (Table 3). Each simulation involved the injection of air (79% non-condensable gas and 21% oxygen, in terms of reaction components) from the injector well. This causes the immobile hydrocarbon (heavy oil and light oil) to burn (equations 2 and 3). Fuel (coke) is the result of cracking reactions (equation 1), which is then, in turn, burnt via the combustion reaction (equation 4) (Burger 1972; Crookston *et al.* 1979; Coats 1980; CMG 2020).

Table 4. Simulation times for different number of grid blocks

Number of grid blocks	Time for one simulation (s)
10	3.4
20	1.5
50	4.0
100	11.2
200	36.9
500	147.5
1000	429.8

This matrix of 120 models (eight oils, 15 geological models) was created to test how the different oils, with their different physical properties, interact with the range of petrophysical properties, and to specifically test how exothermic oil oxidation varies with porosity, permeability, initial crude oil viscosity and API gravity. Tracking the modelled temperature and location of the fire-front provides an indication of the location of the oil bank and shows a strong correlation with the state of propagation (Liu *et al.* 2021). There are three reported states of combustion zone propagation; these are sustainable state, declined state and extinguished state. The state of the combustion front is an indicator of the degree of success of air injection in models and sustainability of the combustion front for each given set of parameters.

Each simulation was run initially for one year; the temperature profiles were reported and analysed to differentiate the effects of porosity, permeability, API gravity, and initial oil viscosity on the temperature profile and the velocity of the fire-front. The same models were then run for 20 years to measure the peak enthalpy rate and arrival time at the producer well.

Principal component analysis (PCA)

To establish which of the four input variables (porosity, permeability, oil viscosity and API gravity) has the strongest correlation and largest

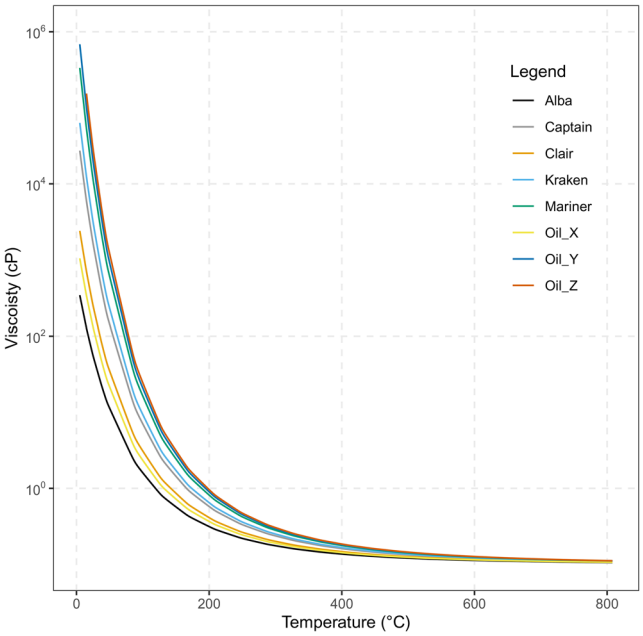

Fig. 4. Viscosity v. temperature graphs to show how the initial oil viscosity of each model decreases with increasing temperature.

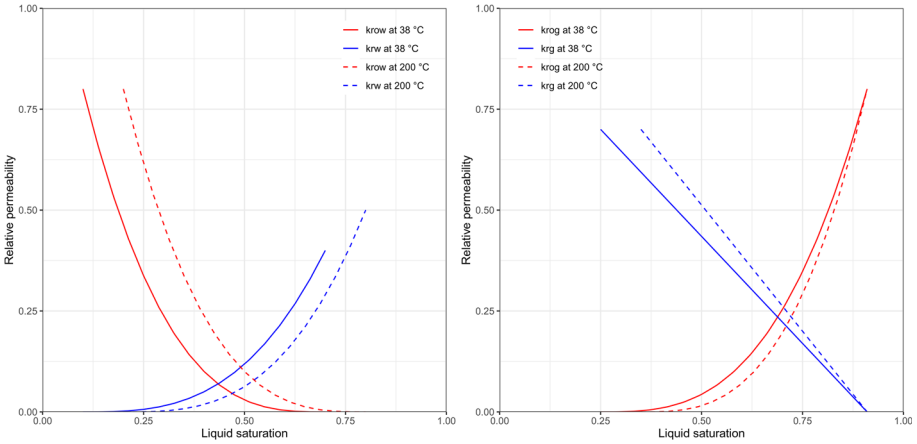

Fig. 5. Relative permeability curves used in all simulations (**a**) oil water relative permeability and (**b**) liquid gas relative permeability curves with temperature dependence included.

effect on each of the four output variables (temperature, velocity, enthalpy rate and final arrival time at the producer well), principal component analysis was used; the data were normalized between 0 and 1 to account for the logarithmic increase in permeability. PCA is a multivariate analysis technique that reduces the dimensionality of the dataset while preserving as much of the variability as possible and so reveals which variables are the dominant controls on the variation in the modelling results (Jolliffe and Cadima 2016).

Results

Porosity models

Increasing porosity shows a general trend of increasing temperature in all cases, with the lowest temperatures always observed in model-1 (10% porosity) between 298 (Fig. 6c) and 383°C (Fig. 6f). The highest temperatures are at 30% porosity in all cases, the highest of which is Oil_Z-5 (Fig. 6e) at 427°C. The difference between the lowest and highest peak temperatures modelled differs between the different oil models (Fig. 6). The smallest difference between the lowest and highest is observed between Oil_X-1 and Oil_X-5 at 22°C (Fig. 6a); the largest range is between Oil_Y-1 and Oil_Y-5, with a range of 91°C (Fig. 6d). The overall effect of increasing porosity is to increase the temperature of the fire-front, the magnitude of this effect is dependent on the oil model, with the smallest difference in one of the lowest API gravity models (10°API) models and the largest difference in one of the highest (20°API), with the rest in between.

In all cases, there is a decrease in velocity observed with an increase in porosity (Fig. 6). The lowest velocity is seen at 30% porosity in all models (Fig. 6a), between 14.25 (Oil_X and Z)

Table 5. Reaction stochiometry and reaction kinetics for the different oil models

		Reaction stochiometry		Reaction kinetics		
		a_1	b_1	Ea_1 (J mol^{-1})	A_1 (day^{-1} kPa^{-1})	H_1 (J mol^{-1})
Equation 1	**Alba**	2.30	19.12	$2.10 \times 10^{+05}$	$3.34 \times 10^{+16}$	0
	Captain	2.36	19.40	$2.10 \times 10^{+05}$	$3.34 \times 10^{+16}$	0
	Clair	1.96	16.17	$2.10 \times 10^{+05}$	$3.34 \times 10^{+16}$	0
	Kraken	3.10	25.44	$2.10 \times 10^{+05}$	$3.34 \times 10^{+16}$	0
	Mariner	2.83	23.27	$2.10 \times 10^{+05}$	$3.34 \times 10^{+16}$	0
	Oil X	3.41	28.03	$2.10 \times 10^{+05}$	$3.34 \times 10^{+16}$	0
	Oil Y	2.24	18.45	$2.10 \times 10^{+05}$	$3.34 \times 10^{+16}$	0
	Oil Z	3.41	28.03	$2.10 \times 10^{+05}$	$3.34 \times 10^{+16}$	0

		Reaction stochiometry				Reaction kinetics		
		w_2	x_2	y_2	z_2	Ea_2	A_2	H_2
Equation 2	**Alba**	24.34	14.83	18.65	2.97	$1.22 \times 10^{+05}$	$2.13 \times 10^{+12}$	$2.01 \times 10^{+07}$
	Captain	24.70	15.10	18.92	3.00	$1.23 \times 10^{+05}$	$2.29 \times 10^{+12}$	$2.01 \times 10^{+07}$
	Clair	20.59	12.51	15.87	2.50	$1.14 \times 10^{+05}$	$9.22 \times 10^{+11}$	$2.01 \times 10^{+07}$
	Kraken	32.39	19.80	24.62	3.96	$1.37 \times 10^{+05}$	$8.89 \times 10^{+12}$	$2.01 \times 10^{+07}$
	Mariner	29.63	18.10	22.57	3.62	$1.32 \times 10^{+05}$	$5.69 \times 10^{+12}$	$2.01 \times 10^{+07}$
	Oil X	35.69	21.84	27.10	4.37	$1.42 \times 10^{+05}$	$1.44 \times 10^{+13}$	$2.01 \times 10^{+07}$
	Oil Y	24.50	14.30	18.02	2.86	$1.21 \times 10^{+05}$	$1.78 \times 10^{+12}$	$2.01 \times 10^{+07}$
	Oil Z	35.69	21.84	27.10	4.37	$1.42 \times 10^{+05}$	$1.44 \times 10^{+13}$	$2.01 \times 10^{+07}$

	Reaction stochiometry				Reaction kinetics		
	w_3	x_3	y_3	z_3	Ea_3	A_3	H_3
Equation 3	2.25	1.19	2.22	0.24	$5.34 \times 10^{+04}$	$4.86 \times 10^{+11}$	$2.16 \times 10^{+06}$

	Reaction stochiometry				Reaction kinetics		
	w_4	x_4	y_4	z_4	Ea_4	A_4	H_4
Equation 4	1.00	0.73	0.44	0.15	$3.41 \times 10^{+04}$	$2.49 \times 10^{+05}$	$2.00 \times 10^{+05}$

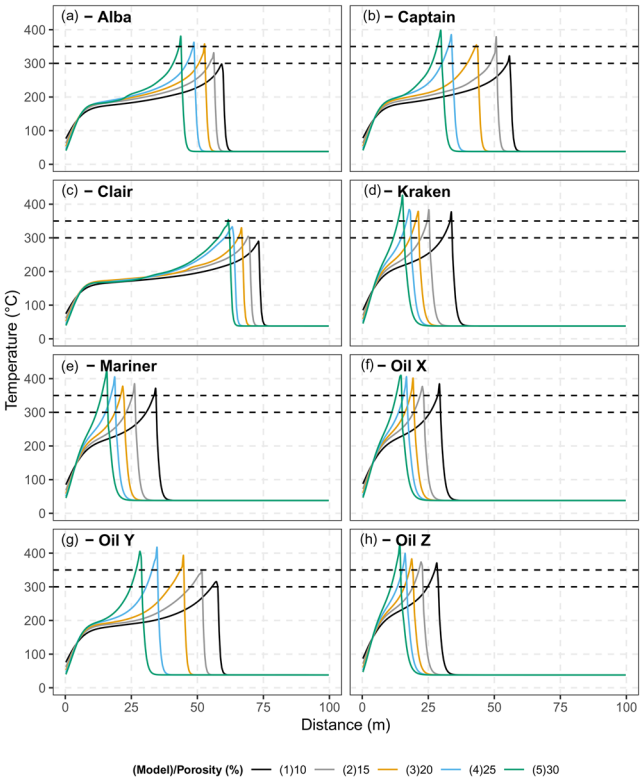

Fig. 6. Temperature profiles over distance between injector and producer for petrophysical models 1 to 5, for all fluid models (varying porosity with a fixed permeability) after one year of simulation. Temperature profiles reveal the peak temperature achieved and the progress and location of the fire-front and how different oil models are affected by different porosity values. (**a**) Alba, (**b**) Captain, (**c**) Clair, (**d**) Kraken, (**e**) Mariner, (**f**) Oil_X, (**g**) Oil_Y, (**h**) Oil_Z. See Table 2 for oil properties. Dashed lines indicate the bounds of the fuel deposition (MTO) reaction zone, 300 to 350°C. Temperature profiles show that, in most cases, porosity is directly related to peak temperature and velocity, with increasing porosity there is increasing peak temperature and decreasing velocity.

(Fig. 6f, g) and 61.75 m yr^{-1} (Clair-5) (Fig. 6c). The highest velocity is observed at 10% porosity for all cases, between 28.25 (Oil_Z-1) (Fig. 6h) and 73.25 m yr^{-1} (Clair-1) (Fig. 6c). The difference between the lowest and highest velocity observed varies depending on the oil model. The smallest difference (11.5 m yr^{-1}) is observed between Clair-1 (10% porosity) and Clair-5 (30% porosity) (Fig. 6a); the largest difference (29 m yr^{-1}) is seen between Oil_Y-1 and Oil_Y-5 (Fig. 6g).

There is less clear of a pattern between enthalpy rate and porosity (Fig. 7), the highest enthalpy rates generally occur in rocks with greater than 25% porosity for all the oils with the exception of Oil_Z (Fig. 7d), in which it occurs at 20%. There is, however, no clear pattern of increasing enthalpy with increasing porosity.

The arrival time of the fire-front at the producer is increasingly late at higher porosities in each set of models (Fig. 7), with the earliest arrival times, of around 2 years, being in model-1 (10%) porosity and the latest being in model-5 (30%) porosity. The difference between the earliest and latest arrival time varies between oil models, with the difference between Clair-1 and -5 being less than a year to 1 year; Alba-1 to -5 being 1 year, and all others being 2 years.

The output from these models reveals how reservoirs with variable porosity but constant, or similar, permeability (in the model, 1000 mD) influence exothermic oil oxidation. Barring some exceptions described above, for a fixed permeability, higher porosities generally give lower velocities and therefore later arrival times and higher fire-front temperatures, the relationship with enthalpy is however unclear.

Permeability models

Models of variable permeability (Fig. 8) show that in all cases of model-6 (1 mD permeability) the temperature never exceeds 307°C. All models show a sharp increase in temperature between 1 and 10 mD permeability, from 49°C between Clair-6 and -7 and 94°C for Oil_Z-6 and -7. Temperatures for Alba and Clair peak at 10 mD; Kraken, Mariner, Oil_X, Oil_Y and Oil_Z display a small increase up to 100 mD; Captain peaks at 1000 mD; higher than these permeabilities (up to 10 000 mD) there is negligible increase in temperature in all models (Fig. 8). In all cases except Captain, there is a negligible difference (between 1 and 16°C) between the peak temperature observed between model-9 and -10 (1000 to 10 000 mD permeability), with Captain showing a difference of 41°C. The highest temperature overall is observed in Mariner-8 (100 mD permeability) at 390°C. The difference between the lowest and highest peak temperature observed across these models varies depending on the oil model, with the smallest range (39°C) seen between Clair-6 and -7 (Fig. 8b) (1 to 100 mD permeability) and the largest range (94°C) seen between Oil_Z-6 and -8 (Fig. 8h) (1 to 1000 mD permeability).

In all cases the lowest velocity is observed in model-6 (1 mD) between 3.75 m yr^{-1} (Mariner-6 and Oil_Z-6) and 5.75 m yr^{-1} (Alba-6 and Clair-6) and the highest velocity is seen in model-10 (10 000 mD) between 22.75 m·yr^{-1} (Oil_X-10 and Oil_Z-10) and 69.75 m yr^{-1} (Clair-10) (Fig. 8). The smallest range between lowest and highest velocity models (18 m yr^{-1}) is between Oil_X-10 and -6, and the largest range (64 m yr^{-1}) is seen between Clair-10 and -6.

The highest enthalpy rates are observed in Alba-6, Captain-6 and Clair-6 (Fig. 9a); with the exception of Oil_X, these are the only models to reach the production well within 20 years at 1 mD permeability. Oil_X shows its peak enthalpy rate at 10 mD permeability (Fig. 9b), slightly higher than that observed at 1 mD (Fig. 9a). The remaining oil models show their peaks at different permeabilities and display no clear pattern (Fig. 9). The highest peak enthalpy rates observed are those that reach the production well at 1 mD permeability (Fig. 9a).

The latest arrival time for the thermal front is always in model-6, taking between 10 and 15 years in the models that do arrive, and over 20 in all others (Fig. 9a). The earliest arrival time at the production well is variable but is generally in geo-models with permeability >100 mD in all cases, with the exception of Oil_X, in which it is at 10 mD.

The results of these models reveal how variable permeability, with no porosity dependency, influence the ISC process such that for a fixed porosity, higher permeability gives higher fire-front velocities, though this is not a linear relationship. Temperature and enthalpy rate peak generally between 1 and 10 mD permeability and show a small decrease thereafter.

Carman–Kozeny models

In this section, the effect on fire-front properties as a function of the covariation of permeability and porosity has been modelled, defined using equation (5), at set porosities between 10 and 30%. These models (Fig. 10) show peak temperature increases with increasing porosity and permeability. The lowest peak temperature is observed in model-11 (10% porosity and 278 mD permeability) (Fig. 10), in all cases bar Oil_Z, where the lowest peak temperature is observed within model-12 (15% porosity and 1052 mD permeability). Overall, the highest peak fire-front temperature is observed in Oil_Z-15 (30% porosity and 12 407 mD permeability) at 422°C (Fig. 10e). The smallest difference between lowest and highest peak temperature (28°C) for an oil model is observed between Kraken-11 and -15; the largest difference (67°C) is observed between Captain-11 and -15.

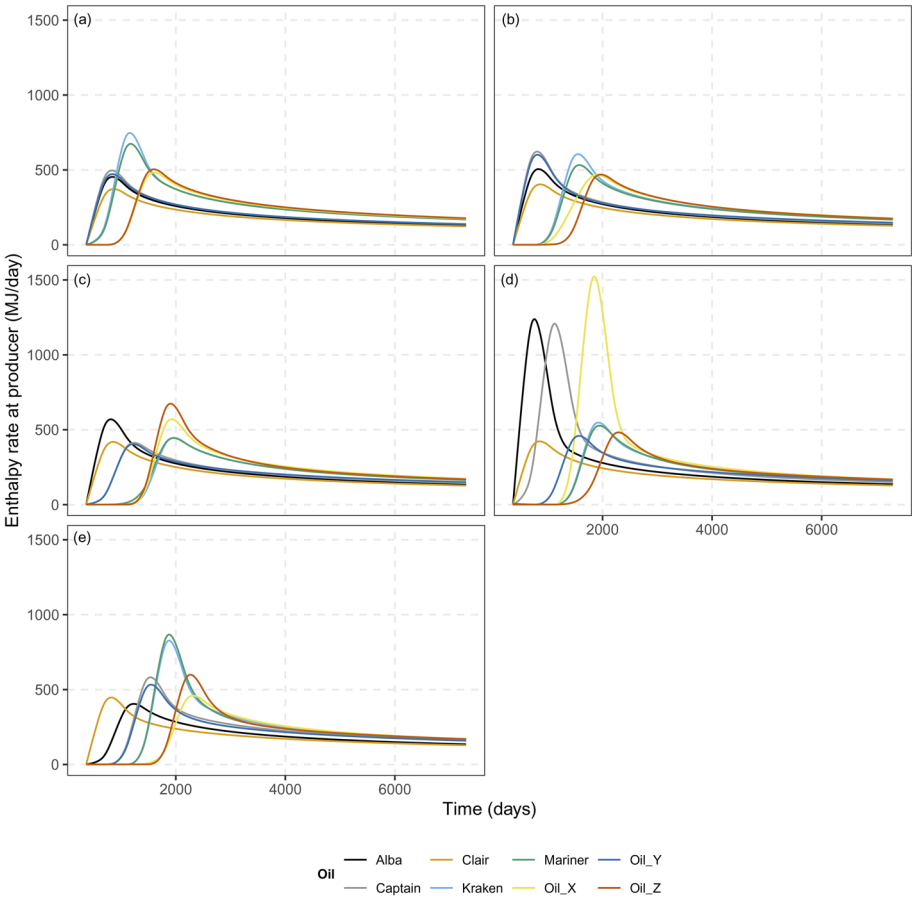

Fig. 7. Graph of enthalpy rate over time for each model 1 to 5, 1000 mD permeability and variable porosity, with oil models coloured. (**a**) model 1–10% porosity, (**b**) model 2–15% porosity, (**c**) model 3–20% porosity, (**d**) model 4 25% porosity, (**e**) model 5–30% porosity.

The lowest velocity for each oil is observed in model-15 (30% porosity, 12 407 mD permeability), between 14.25 m yr^{-1} observed in Kraken-15 to 64.75 m yr^{-1} in Clair-15 (Fig. 10). Conversely the highest peak velocity is observed in model-11 (10% porosity, 278 mD permeability), between 27.75 m yr^{-1} for Oil_Z-11, and 72.25 m yr^{-1} for Clair-11. The difference between the lowest and highest peak velocity between different oil models is variable, with the smallest difference observed between Clair-11 and 15 at 7.50 m yr^{-1}, and the largest at 22 m yr^{-1} between Captain-11 and -15 (Fig. 10).

There is no clear pattern between enthalpy rate and porosity and permeability change in the Carman–Kozeny models (Fig. 11), although they do seem to be slightly lower than the equivalent porosity models (Fig. 7). The same is observed with the relative arrival times of the fire-front.

Principal component analysis of the controlling factors on *in situ* combustion processes

Porosity models

For the porosity-variation models (models 1–5), porosity accounts for most of the variation in PC1 and the viscosity and API gravity of the oil account for an even input on both PC1 and PC2 (Fig. 12a). In these models, there is a moderately strong correlation between porosity and temperature, with a large change in porosity accounting for a comparatively small change in temperature. There is also a moderate negative correlation between API gravity and temperature, with a larger change in API gravity required than that of porosity, to influence the peak temperature.

There is a strong positive correlation between API gravity and velocity and a moderate negative correlation between porosity and velocity. A small variation in API gravity is responsible for a comparatively large variation in velocity, compared to comparatively larger variation in porosity accounting for a smaller change in the velocity. The correlation between porosity and peak enthalpy rate is moderately strong, with a small change in enthalpy resulting from a large change in porosity. There is also a strong negative correlation between API gravity and arrival time. In these models the variable that is mostly responsible for the changes in temperature is porosity as it has the best correlation while the biggest influence on velocity is the API gravity of the oil (Fig. 12a).

Permeability models

For the permeability-variation models (models 6–10), the variation in both PC1 and PC2 is jointly accounted for by petrophysical and oil physical properties (Fig. 12b). There appears to be no direct correlation between permeability and temperature in these models. There is a very weak positive correlation between viscosity and temperature, and a very weak negative correlation with API gravity, a smaller variation in API gravity, compared with viscosity, accounts for the change in temperature. Permeability and API gravity have moderately strong positive correlations with velocity, and initial oil viscosity has a moderately strong negative correlation with velocity. API gravity shows the smallest observed variation with regards to the change in velocity, with permeability and viscosity showing a similar effect on the velocity. In these models, there is a strong negative correlation between permeability and arrival time for the fire-front, and a strong negative correlation between viscosity and peak enthalpy rate.

Carman–Kozeny models

There is a moderate positive correlation between initial oil viscosity and temperature, as well as a moderate positive correlation between porosity and permeability with temperature. There is also a strong negative correlation between temperature and API gravity; the smallest variation of API gravity causes the greatest change in temperature,

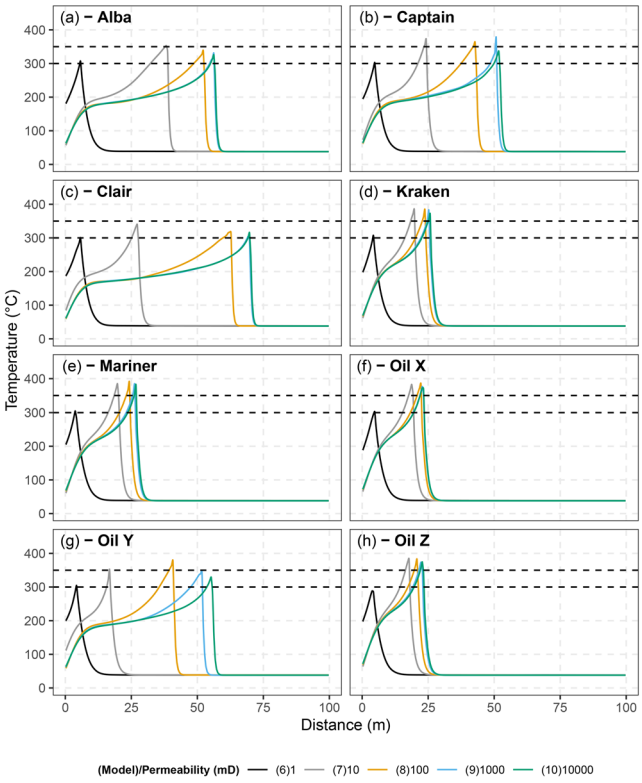

Fig. 8. Temperature profiles over distance between injector and producer for petrophysical models 6 to 10, for all fluid models (varying permeability for fixed porosity) after one year of simulation. Temperature profiles reveal the peak temperature achieved and the progress and location of the fire-front and how different oil models are affected by different permeability values. (**a**) Alba, (**b**) Captain, (**c**) Clair, (**d**) Kraken, (**e**) Mariner, (**f**) Oil_X, (**g**) Oil_Y, (**h**) Oil_Z. See Table 2 for oil model properties. Dashed lines indicate the bounds of the fuel deposition (MTO) reaction zone, 300 to 350°C. Temperature profiles show permeability is weakly related to temperature at permeabilities greater than 1 mD, with a large increase in temperature between 1 and 10 mD and a slight decrease thereafter. Permeability is strongly related to the velocity of the fire-front, with increasing velocity as permeability increases.

porosity is the second-most important control on temperature in this set of models (Fig. 12c). For the models of co-varying porosity and permeability, there is a very strong positive correlation between API gravity and velocity, and a strong negative correlation between initial oil viscosity and velocity. In these models there is a weak negative correlation between porosity and permeability and velocity.

Peak enthalpy rate shows a strong positive correlation with viscosity, and a strong negative correlation with API gravity. Arrival time is strongly correlated with velocity, which in turn is mostly controlled by the oil physical properties rather than the petrophysical properties of the reservoir.

Discussion

The effect of porosity and permeability on the *in situ* combustion processes

Maximum temperature

Porosity and permeability have both individual and combined effects on the maximum temperature of the fire-front. Increasing porosity up to 30% increases the maximum temperature of the fire-front (Fig. 6); this is a result of a greater proportion of the rock taken up by pores which leads to a greater volume of oil within a unit volume of the rock (Tiab and Donaldson 2015). The greater volume of oil per unit volume of rock allows for the deposition of more fuel (coke), thus resulting in greater temperatures being reached during the subsequent coke combustion reactions (equation 4).

Model-6 (15% porosity, 1 mD permeability) (Fig. 8) restricts the temperature to below 310°C for all oil types (Fig. 8). This relatively low temperature is insufficient to initiate deposition of coke to any significant degree during MTO (300 to 350°C), which therefore obviates the burning of coke (equation 4) to any substantial degree, limiting the temperature and preventing it from reaching 350°C and undergoing HTO reactions (Ranjbar and Pusch 1991). This means LTO reactions dominate the ISC process in ultra-low permeability models (<10 mD), thus preventing the temperature reaching higher values, leading to a declined state of propagation, which may be sustainable only if air injection rates and air flux are correctly managed and monitored (Ren *et al.* 2002).

For Alba, Clair and Oil_X at 100 mD permeability, the temperature increases sufficiently to allow for more fuel deposition than there is below 10 mD, but for Alba and Clair the temperature does not exceed 350°C and therefore does not undergo HTO reactions to any substantial degree (Fig. 8a, c). Captain, Kraken, Mariner, Oil_Y and Oil_Z exceed 350°C above 100 mD permeability and do undergo HTO reactions, this is also observed in experimental models with lighter oils (such as Alba and Clair) exhibiting lower temperatures in general (Askarova *et al.* 2020).

When porosity and permeability are co-varied in the models, the results are similar to the simple increase in porosity (Fig. 6), with the overall consequence being an increase in temperature with increasing porosity, although this increase is less pronounced than it is in models 1 to 5. In models with greater than 100 mD permeability the peak temperatures do not greatly vary (Fig. 10), e.g. for the same porosity, models 1 to 5 are, in all cases, hotter than models 11–15, e.g. Kraken-5 (30% porosity and 1000 mD permeability) reaches 426°C but Kraken-15 (30% porosity and 12 407 mD) reaches only 402°C. At high permeabilities there is a slight restriction in peak temperatures for the given porosity.

Fire-front velocity

Porosity increase at fixed permeability serves to decelerate the fire-front (Fig. 6); this is because elevated pore space leads to a greater volume of oil within the rock, therefore greater volume of fuel (coke), which will take longer to burn, and using more oxygen (note that all models inject air at the same rate), therefore slowing the reaction rate and slowing the progress of the fire-front. Increasing permeability at fixed porosity has the opposite effect on the fire-front velocity (Fig. 8), as increasing permeability, and thus the ability of the reactive fluid to flow through the rock (Tiab and Donaldson 2015), increases the velocity. Faster fluid flow results in a higher velocity of the fire-front.

When porosity and permeability are co-varied (models 11 to 15), the velocity slows down similar to the behaviour of increasing only the porosity alone (models 1 to 5) (Fig. 6). We can deduce that the effect of porosity increase on velocity overrides the effect of permeability increase. It is worth noting that there is only a ten-fold increase in velocity for an increase of five orders of magnitude of permeability. The difference between Clair-5 (30% porosity, 1000 mD permeability) and Clair-15 (30% porosity, 12 407 mD permeability) shows a slight increase in velocity (61.75 to 64.75 m yr^{-1}), a difference of 3 m yr^{-1} with an order of magnitude increase in permeability; there is no difference in velocity for Alba, Kraken or Mariner when permeability increases from 1000 to 12 407 mD.

Enthalpy and arrival time

When only porosity is varied (models 1 to 5) there is a similar correlation between porosity and temperature as there is between

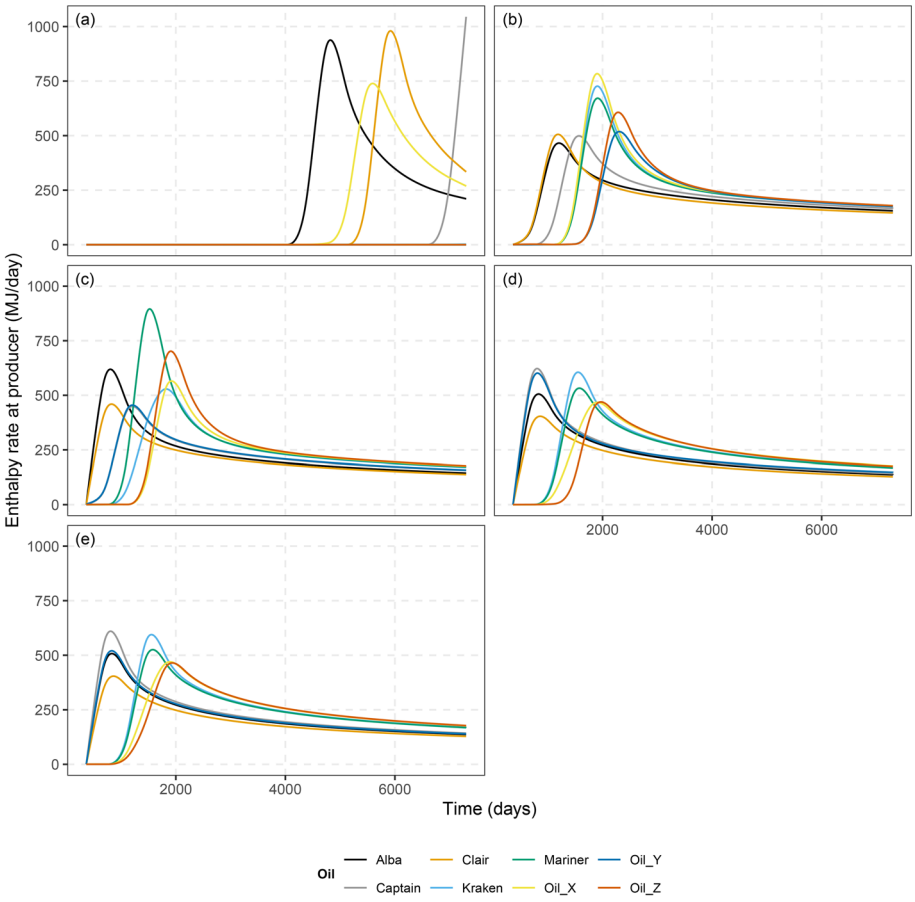

Fig. 9. Graph of enthalpy rate over time for each model 6 to 10, variable permeability and 20% porosity, with oil models coloured. (**a**) Model 6–1 mD permeability, (**b**) model 7–10 mD permeability, (**c**) model 8–100 mD permeability, (**d**) model 9–1000 mD permeability, (**e**) model 10–10 000 mD permeability.

porosity and enthalpy rate; with increasing porosity there is an increasing enthalpy rate and an almost identical effect on the arrival time (Fig. 7). There is therefore a strong link between temperature and enthalpy rate and velocity with arrival time in these models (Fig. 12a). When porosity and permeability are co-varied (models 11 to 15), the output is less straight forward and oil physical properties have a significant influence (Fig. 12c). Therefore, when there is large variations in permeability, the oil physical properties become more important for the enthalpy rate and the arrival time. Ultimately, and as expected, the velocity is the dominant control on arrival time (Figs 12, 13), and there is no clear correlation between the petrophysical properties and the enthalpy rate in cases where permeability and porosity vary. The observed difference in the enthalpy rate with changing permeability is most likely to be due to the fire-front not arriving at the producer well in the 1 mD model, in some cases, therefore there is no meaningful peak enthalpy rate for those models (Fig. 9a). The models that do reach the production well at 1 mD have higher peak enthalpy rates than the same oil model in reservoirs that have permeability greater than 1 mD. The low temperature fire-fronts observed in models at 1 mD permeability, (model-6) (Fig. 9a) suggests that these may be the least suitable for geothermal exploitation, however, when they do reach the producer, these ultra-low permeability models show the highest peak enthalpy rates. The high enthalpy rates would be preferential for any kind of EGS system in terms of overall energy production, however, with arrival times in excess of 16 years, these types of reservoirs may take too long to commercially produce energy on the required scale. With far earlier arrival times observed in models over 100 mD, (2 to 5 years) (Fig. 9b–e), these higher permeability reservoirs may prove far better to work with in terms of short to medium term energy production, as the fire-front arrival time is far earlier.

The effect of viscosity and density on *in situ* combustion processes

Maximum temperature

The maximum peak temperature of the fire-front for all oil types shows a strong positive correlation with initial oil viscosity and API gravity (Figs 12, 13). The observed increase in temperature with initial oil viscosity in the oil models can be attributed to fluid flow rates, as Darcy's law states that flow rate is inversely proportional to viscosity (Tiab and Donaldson 2015). Slower flow rates result in the oil having more time, *in situ*, to undergo fuel deposition reactions, therefore depositing more fuel, which in turn burns via HTO reactions, reaching the highest temperatures observed in the oils with highest initial viscosity; this effect diminishes with ever increasing initial oil viscosity. The observed increase in temperature with API gravity can be attributed to the greater number of carbon atoms in the heavy oil component allowing for a greater number of molecules of coke (Table 5) to be deposited, allowing for more fuel for the HTO reactions. PCA reveals that a smaller change in API gravity accounts for a greater change in temperature than that of viscosity (Figs 12, 13).

Fire-front velocity

The velocity of the fire-front decreases with increasing initial oil viscosity (Figs 12, 13), because viscosity is a measure of a fluid's resistance to change shape, or, in this case, flow. High viscosity fluids flow through porous media more slowly than low viscosity fluids, according to Darcy's Law. High viscosity slows the movement of the preceding zones (coking zone, cracking zones, steam plateau, water bank and oil bank) through the reservoir, therefore slowing down the zones of fuel (coke) deposition and therefore the propagation of the fire-front though the reservoir.

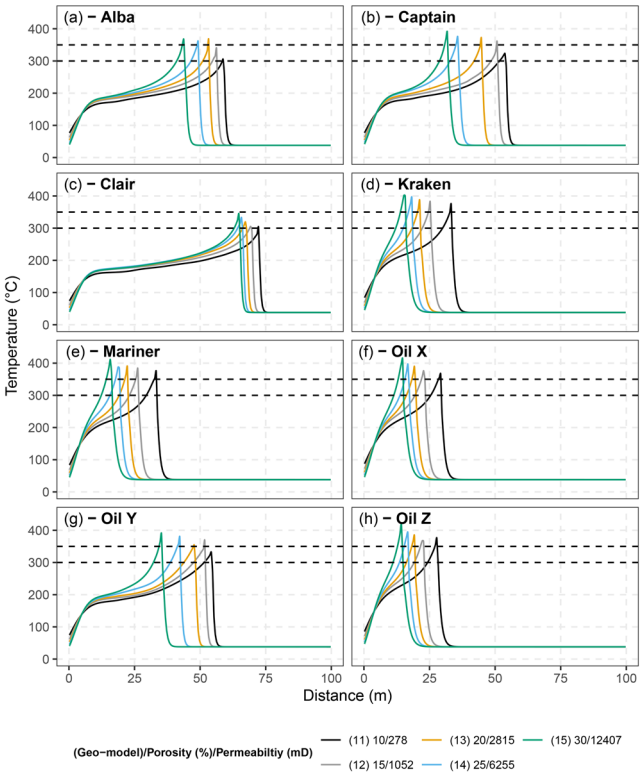

Fig. 10. Temperature profiles over distance between injector and producer for petrophysical models 11–15, for all fluid models after one year of simulation. Temperature profiles reveal the peak temperature achieved and the progress and location of the fire-front and how different oil models are affected by different porosity and permeability values, governed by a simplified Carman–Kozeny relationship. (**a**) Alba, (**b**) Captain, (**c**) Clair, (**d**) Kraken, (**e**) Mariner, (**f**) Oil_X, (**g**) Oil_Y, (**h**) Oil_Z. See Table 2 for oil model properties. Dashed lines indicate the bounds of the fuel deposition (MTO) reaction zone, 300 to 350°C. Temperature profiles show that, in most cases, porosity is directly related to peak temperature and velocity, with increasing porosity there is increasing peak temperature and decreasing velocity, such is observed in Figure 6, however there is a minor influence observed from the increased permeability seen in models 14 and 15, with a small increase in velocity as compared with models 4 and 5.

The API gravity of the oil shows a strong positive correlation with velocity (Figs 12, 13). Higher density (lower API gravity) oils have lower fire-front velocities (Figs 6, 8 and 10). In the reaction scheme employed, the lower API gravity oils have greater numbers of carbon atoms taking part in the fuel deposition reaction (Table 5), therefore there is a greater amount of fuel (coke) laid down. Elevated volumes of fuel take longer to burn, therefore slowing the advancement of the fire-front and the zones in front, the opposite is true for lower volumes of fuel, this is seen experimentally in combustion tube models also (Crookston *et al.* 1979).

Enthalpy and arrival time

The overall effect of varying oil properties on the enthalpy rate at the production well appears to be a combined consequence of viscosity and API gravity (Figs 12, 13). Viscosity generally shows a stronger correlation than API gravity with enthalpy rate (Fig. 13). A small change in API gravity has a more significant effect on enthalpy rate, whereas, in comparison, a small change in viscosity has a minor effect on enthalpy rate (Fig. 13). The fire-front arrival time is directly correlated with the velocity, as expected; therefore, the controls on velocity and arrival time are the same (Figs 12, 13). At 1 mD permeability, the velocities observed are so low that, even at 20 years, only the very fast-moving fronts in the low viscosity and high API gravity oils reach the production well (Fig. 9a). Oil_X (46 cP) has two orders of magnitude higher viscosity than Oil_Z (4664 cP), for the same low API gravity (10°API); Oil-Z never reaches the production well at 1 mD permeability whereas Oil_X does, this is reflected in the increase in enthalpy rate (Fig. 9a).

Combined effects of petrophysics and oil physical properties on *in situ* combustion processes

The consequence of changing petrophysical properties is not identical across the different oil models (Figs 6, 8 and 10). For model-1 (10% porosity), the peak temperature is between 286 (Clair) and 375°C (Kraken) (Fig. 5), a difference of 90°C. In contrast, the peak temperatures at 30% porosity (model 5), is between 353 (Clair) and 426°C (Kraken), a difference of 72°C (Fig. 6a, e). This resulting temperature range difference of 18°C shows that, for high porosity cases, the effect of initial oil viscosity on temperature is relatively weak; oil physical properties are more influential at low than high porosities (Figs 6, 10).

There is a difference between the lowest and highest peak temperature observed between the same oil model between 10 and 30%; the largest difference seen is 90°C, seen in Oil_Y (20°API), and the smallest difference is 22°C, seen in Oil_X (10°API), the rest sit between with some variation, however, the general trend shows for higher API gravity models, there is greater affect from porosity on temperature (Fig. 6).

When just porosity is varied (models 1 to 5) there is a correlation between porosity and enthalpy rate (Fig. 12a), however, when permeability variation is introduced (models 6 to 15) (Fig. 12b, c) there is strong input from the API gravity and viscosity of the oil that is not seen in models 1 to 5.

Models that do not reach substantially higher than 300°C are not sufficiently hot enough to begin coke (fuel) deposition and therefore coke combustion (>350°C) to any meaningful degree (Figs 6a, c and 8a–e). This shows that in situations of low porosity (≤10%) or low permeability (≤10 mD) with the lighter oils (Alba and Clair) (Fig. 6a, c), there is little fuel deposition, and the process is dominated by LTO reactions. If such a situation as this should arise in a field application, it is important that the oxygen is consumed in low temperature oxidation reactions to prevent oxygen bypass and the dangerous co-production of volatile oil and oxygen (Fassihi *et al.* 1990). In practice, such situations of dominance by LTO reactions and oxygen bypass may present problems with stable fire-front propagation across the reservoir if the oxygen concentrations are not correctly monitored (Fassihi *et al.* 2016) therefore any factors, whether chemical or petrophysical, that control whether the LTO reactions or HTO reactions are dominant, must be properly understood prior to field operation. This being said, there have been successful projects in such reservoirs including: The Buffalo field; Cedar Hills; Medicine Pole Hills and Pennel (Kumar *et al.* 1995; Gutiérrez *et al.* 2009; Ling *et al.* 2014), showing that with careful preparation and monitoring, highly successful ISC projects are possible. The success of these projects has been attributed to a robust project design workflow using experimental data an numerical modelling (Storey *et al.* 2022).

Overall controls

Principal component analysis on all the models (Fig. 13) revealed that overall the variance in temperature is controlled mostly by the initial oil viscosity and API gravity; this is followed closely by porosity and then permeability. However, porosity and API gravity show a smaller magnitude difference appears to have a greater effect on temperature than that of permeability or viscosity, making them the primary controls on peak temperature.

The velocity of the fire-front is mostly controlled by the viscosity and API gravity of the oil with little input from porosity and even

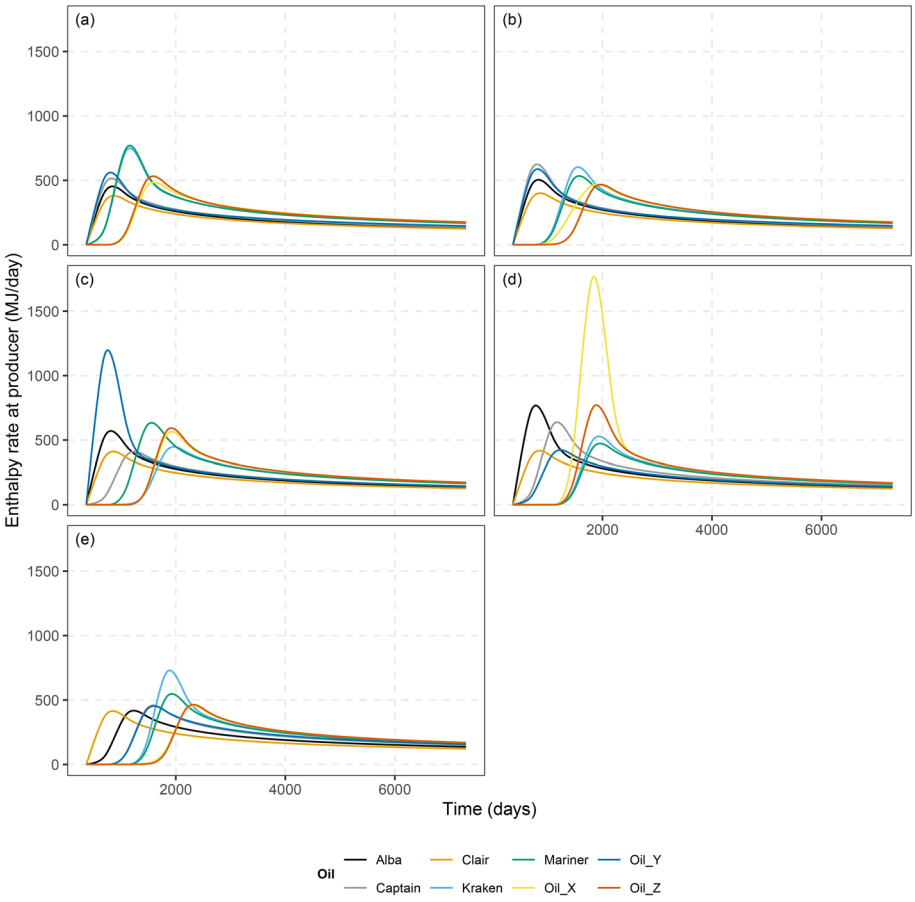

Fig. 11. Graph of enthalpy rate over time for each model 11 to 15, variable permeability and variable porosity, with oil models coloured. (**a**) Model 11–10% porosity, 278 mD permeability, (**b**) model 12–15% porosity, 1052 mD permeability, (**c**) model 13–20% porosity, 2815 mD permeability, (**d**) model 14–25% porosity, 6255 mD permeability, (**e**) model 15–30% porosity, 12 407 mD permeability.

less input from permeability; this is shown by the majority of variation in PC1 being controlled by the API gravity and initial oil viscosity (Fig. 13), Thus, permeability has little to no correlation with velocity when other parameters, such as porosity are also varied (Fig. 13), revealing the dominant control of porosity and API gravity on velocity. In practice, and in Alba, Captain, Clair and Kraken models, the viscosity of the oil is related to the API gravity of the oil, however, the chemical make-up of the oil, described by the Watson characterization factor, also influences the viscosity of the oil (Watson *et al.* 1935). Thus, the viscosity of the oil can increase with no change in API gravity and vice versa. To be clear, the specific chemistry of the oil has not been explicitly modelled in this study. Oil_X, Oil_Y and Oil_Z have been used to offset the relationship between API gravity and viscosity and have revealed that API gravity has a marginally stronger influence on both temperature and velocity than viscosity (Fig. 13).

The arrival time of the fire-front at the production well is entirely dictated by the velocity of the fire-front, and therefore has the same overall controls as velocity. The overall controls on peak enthalpy rate are less clear; PCA (Figs 12, 13) suggests that peak enthalpy rates are dictated by a combination of temperature and velocity of the fire-front, with the velocity being controlled by API gravity and viscosity. The oil physical properties therefore dictate the enthalpy rate at the producer well in the absence of a petrophysical difference. The residence time of the oil, and enthalpy it carries, are the controlling factor on the peak enthalpy rates (Figs 7, 9 and 11), so lower velocity fire-fronts are able to reach higher peak enthalpy rates; this effect is related to the Damköhler number, which has been

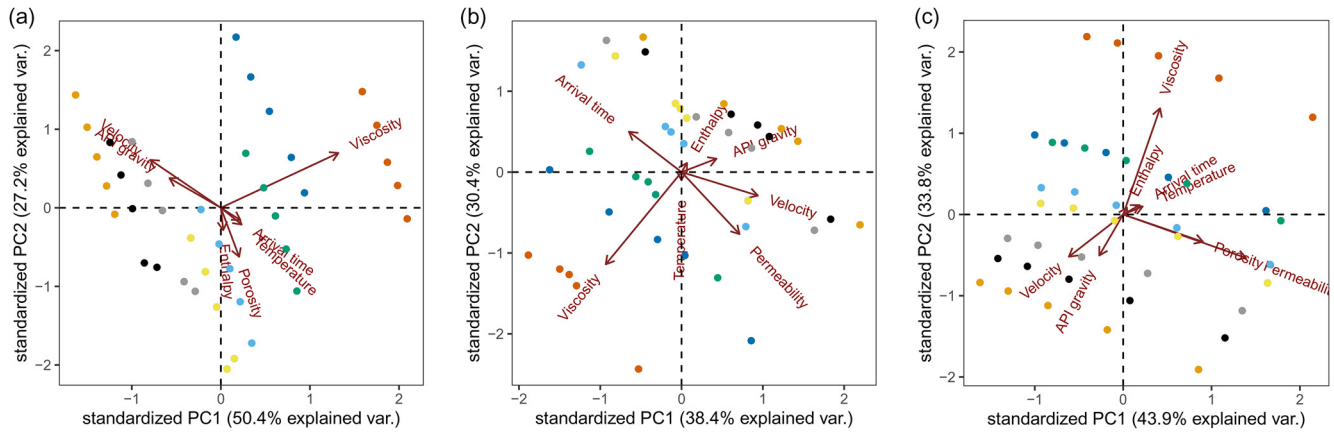

Fig. 12. Principal component analysis biplot showing how principal components 1 and 2 are affected by the model variables. (**a**) Porosity models 1–5. (**b**) Permeability models 6–10. (**c**) Carman–Kozeny models 11–15.

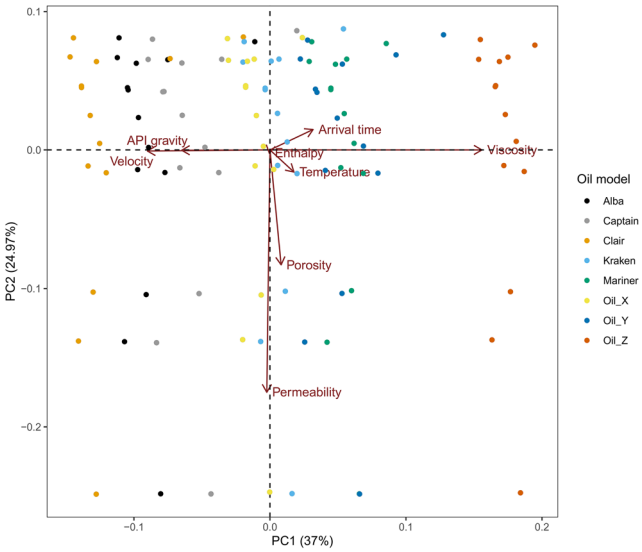

Fig. 13. Principal component analysis biplot showing how principal components 1 and 2 are affected by the model variables with all data used in the analysis for models 1–15.

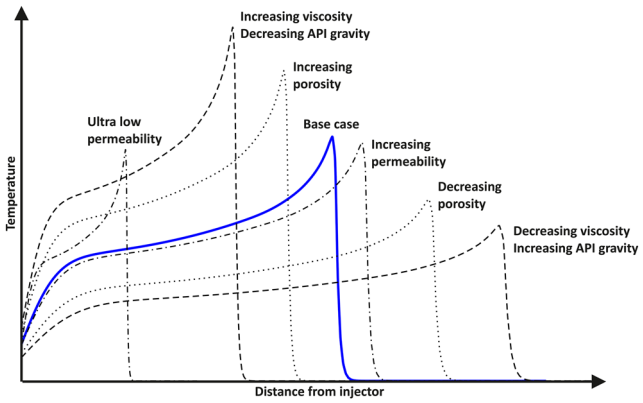

Fig. 14. Schematic diagram to illustrate the broad effects of porosity, permeability, initial oil viscosity and API gravity on the temperature profile of the fire-front after one year of simulation.

reported to be the most important factor in terms of controls on *in situ* upgrading simulations (Maes *et al.* 2017). The relative importance of the fluid properties, as defined by the Damköhler number in the study by Maes *et al.* (2017), shows that, in terms of peak enthalpy rate, the fluid kinetics are the controlling factor on enthalpy and are not directly correlated with the temperature of the fire-front or the factors that influence it.

Although the PCA analysis suggests that the permeability is the least important factor (Fig. 13), it is worth stating that porosity and permeability are not always directly related; for example the fractured tight sand reservoir in the Buchan Field (Wynn and Saundry 2020), which has low porosity (9% mean) and high permeability (up to 1670 mD), or the fractured chalk reservoir in the Ekofisk Field (Agarwal *et al.* 1997, 2000) which has high porosity (up to 40%) and low matrix permeability (around 1 mD) but locally effective fracture-related permeability. In such cases, permeability would exert a controlling factor on the fire-front temperature and velocity, as demonstrated in models (6 to 10). The specific orientation and width of fractures may have important influences on fire-front temperature and velocity (Fadaei *et al.* 2011; Aleksandrov *et al.* 2017). The specific effects of localized fractures have not been specifically modelled in this study.

Significance and limitations of models

To establish the significance of the simulation results, it is important to relate the findings to real-world examples. The average petrophysical properties of the host reservoir rock of the five North Sea oil models (Table 6) can be used to establish the significance. For enhanced geothermal systems, high temperatures and high enthalpy rates, for greater heat exchange, and low velocities, but not too late an arrival time, for greater duration of the process, are ideal.

Based on the modelling data, Captain, Kraken and Mariner Fields seem to be ideal due to their high porosity and high initial viscosity oils, with permeabilities ranging between 7000 and 10 000 mD. The high velocity of the fire-front caused by the high permeabilities (Fig. 8a–e) may present issues with longevity of the process, although this may be offset by high porosities (in excess of 30%) in these three fields, such as seen in models 14 and 15 (Fig. 10).

In terms of petrophysical properties, Alba would also be suitable, although the low viscosity of the oil would present problems with peak temperature and high fire-front velocity as well as managing the air injection rates and air flux to ensure LTO reactions use up all the oxygen. Clair models present the same problems associated with lighter oils, given the lower fire-front temperatures and higher fire-front velocities observed within Clair models (Figs 6c, 8c and 10c). With the strict monitoring that would be required, it is not the most ideal type of oil field for this application, as well as this, Clair field in general has far lower porosities than seen in the other four (Table 6), further lowering the temperature range, as seen in models 1–3 and 11–13 (Figs 6, 10). This being said, six of the most successful and still currently operating ISC projects in the USA have oils with API gravity between 27 and 38°API and are generally found in low permeability, high porosity reservoirs (Storey *et al.* 2022).

In keeping the models as universal as possible, it is recognized that there are limitations to this simple one-dimensional approach:

(1) One-dimensional models do not truly represent the size or complexity of oil reservoirs or account for heat loss into the adjacent formation.
(2) The simple reactions scheme (equations 1–4) does not fully represent the complex array of reactions occurring during *in situ* combustion; more complex bespoke reaction schemes, perhaps used at later stages of investigation would give more accurate models (Anderson and Kovscek 2022*b*).
(3) The heavy oil component data are based only on viscosity and density of the oil (Fig. 4) and are not based on experimental data. It would be appropriate to create time-

Table 6. Porosity and permeability measurements of the reservoir unit for the five modelled oils

Oil field	Mean porosity (%)	Mean permeability (mD)	Relevant models	Reference
Alba	34.5	2000 to 3000	5, 13, 14, 15	(Moore *et al.* 2020)
Captain	31	7000	14, 15	(Pinnock and Clitheroe 1997)
Clair	12 to 15	<10 to 360 mD (locally fractured)	1, 2, 6, 7	(Robertson *et al.* 2020)
Kraken	36	2000 to 10 000	5, 14, 15	(Parkes *et al.* 2020)
Mariner	33 to 34	2500 to 10 000	5, 14, 15	(Silcock *et al.* 2020)

consuming and expensive experimental data once a suitable reservoir has been selected.

(4) As a result of how the fluid models are made, the API gravity is related to the number of carbon atoms taking place in the reaction, meaning the stochiometry of the reactions vary based on the API gravity of the fluid model (CMG 2020).

(5) The simple relative permeability curves used here (Fig. 5) are not an accurate representation of all reservoirs. Once a candidate field has been selected, reservoir-specific relative-permeability curves should be generated and used in a bespoke model.

However, we consider these simulations to be appropriate for making first order interpretations on the effects of petrophysical properties and oil physical properties to aid in selecting two-dimensional and three-dimensional representations to create more geologically realistic models to aid in selecting appropriate sites for application of such technology.

Conclusions

- The most dominant petrophysical factor controlling both the temperature and velocity of the fire-front is porosity, as greater quantities of oil per unit volume result in more reaction at a given location. Permeability has a variable effect on temperature, with the higher permeabilities leading to lower temperatures as a given volume of oil is increasingly mobile (Fig. 14). When permeability alone is varied (models 6 to 10) the permeability exerts some control on velocity of the fire-front, however, this effect is masked by the effect of porosity when they are covaried (models 11 to 15) (Fig. 14).
- The API gravity of the oil is the dominant physical oil property on the temperature and velocity of the fire-front, although there is a strong effect from the viscosity as well. Although in models in which only permeability is varied (models 6 to 10), the viscosity becomes slightly more important than the API gravity for the temperature, and less so for the velocity (Fig. 14).
- These models reveal that porosity, permeability, initial oil viscosity and API gravity have important individual effects on the overall process (Fig. 14), but the interactions between them can have a compounding effect on the outcome. For example, there is an effect on temperature seen from both petrophysical and oil physical properties, and the effect of oil physical properties is more influential at lower porosities than it is at higher.
- Although it would be expected that higher temperature fire-fronts would carry more enthalpy, it is not the peak temperature that controls the peak enthalpy rates at the producer well. The velocity of the fire-front has a big influence on the peak enthalpy rates observed at the fire-front, as well the time of arrival. Lower velocity fire-fronts have longer residence time within the reservoir, allowing for greater peak enthalpy rates, but they also arrive at the producer well after relatively long time periods compared to higher velocity fire-fronts.
- The strong interactivity of the variables highlights the importance of fully understanding a reservoirs petrophysical (porosity and permeability) and oil physical properties (API gravity and viscosity) prior to selection. Together, these can a be a powerful tool in reducing the number of large, complex 2D or 3D models that need to be simulated prior to field testing.

Nomenclature

MW, molecular weight (kg mol^{-1})
P_c, critical pressure (kPa)
T_c, critical temperature (°C)
KV1, equilibrium coefficient 1 (Kpa)
KV4, equilibrium coefficient 4 (°C)
KV5, equilibrium coefficient 5 (°C)
ρ, density (kg m^{-3})
β, liquid compressibility (kPa^{-1})
α, thermal expansion coefficient ($°C^{-1}$)
μ, viscosity (cP)
Ea, activation energy (J mol^{-1})
A, frequency factor (day^{-1} kPa^{-1})
H, enthalpy (J mol^{-1})
a, b, w, x, y, z, stochiometric coefficients

Subscripts

$_{1–4}$, equation number

Acknowledgements The authors are grateful to the reviewers for their valuable comments that helped improve the manuscript.

Author contributions **BMS**: conceptualization (lead), data curation (lead), formal analysis (lead), investigation (lead), methodology (lead), resources (lead), software (lead), validation (lead), visualization (lead), writing – original draft (lead); **RHW**: conceptualization (equal), formal analysis (equal), funding acquisition (lead), investigation (equal), methodology (equal), project administration (equal), resources (equal), software (equal), supervision (lead), visualization (equal), writing – review & editing (lead); **DDM**: formal analysis (equal), investigation (equal), methodology (equal), supervision (equal), visualization (equal), writing – review & editing (equal); **JW**: formal analysis (equal), investigation (equal), methodology (equal), supervision (equal), writing – review & editing (equal); **JP**: funding acquisition (lead), project administration (lead), supervision (equal); **AK**: conceptualization (lead), funding acquisition (lead), project administration (lead), supervision (equal)

Funding This research received no specific grant from any funding agency in the public, commercial, or not-for-profit sectors.

Competing interests The authors declare that they have no known competing financial interests or personal relationships that could have appeared to influence the work reported in this paper.

Data availability The datasets generated during and/or analysed during the current study are not publicly available due to patents from companies involved but are available from the corresponding author on reasonable request.

References

Ado, M.R. 2022. Comparisons of predictive ability of THAI in situ combustion process models with pre-defined fuel against that having fuel deposited based on Arrhenius kinetics parameters. *Journal of Petroleum Science and Engineering*, **208**, 109716, https://doi.org/10.1016/j.petrol.2021.109716

Agarwal, B., Allen, L.R. and Farrell, H.E. 1997. Ekofisk field reservoir characterization: mapping permeability through facies and fracture intensity. *SPE Formation Evaluation*, **12**, 227–233, https://doi.org/10.2118/35527-pa

Agarwal, B., Hermansen, H., Thomas, L.K. and Sylte, J.E. 2000. Reservoir characterization of Ekofisk Field: a giant, fractured chalk reservoir in the Norwegian North Sea – History Match. *SPE Reservoir Evaluation & Engineering*, **3**, 534–543, https://doi.org/10.2118/68096-PA

Aikman, M.J.L. 2022. Clean energy from oil: a process to generate low cost, low carbon electricity from mature and depleted oil fields. presented at the ADIPEC, 31 October – 3 November 2022, Abu Dhabi, UAE.

Aleksandrov, D., Kudryavtsev, P. and Hascakir, B. 2017. Variations in in-situ combustion performance due to fracture orientation. *Journal of Petroleum Science and Engineering*, **154**, 488–494, https://doi.org/10.1016/j.petrol.2017.02.002

Ambastha, A.K. and Kumar, M. 1999. New insights into in-situ combustion simulation for heavy oil reservoirs. presented at the SPE Annual Technical Conference and Exhibition, Houston, Texas, USA.

Anderson, W.G. 1986. Wettability literature survey - part 1: rock/oil/brine interactions and the effects of core handling on wettability. *Journal of Petroleum Technology*, **38**, 1125–1144, https://doi.org/10.2118/13932-pa

Anderson, W.G. 1987. Wettability literature survey - part 6: the effects of wettability on waterflooding. *Journal of Petroleum Technology*, **39**, 1605–1622, https://doi.org/10.2118/16471-pa

Anderson, T.I. and Kovscek, A.R. 2022*a*. Optimization and uncertainty quantification of in situ combustion chemical reaction models. *Fuel*, **319**, 123683, https://doi.org/10.1016/j.fuel.2022.123683

Anderson, T.I. and Kovscek, A.R. 2022*b*. Analysis and comparison of in-situ combustion chemical reaction models. *Fuel*, **311**, https://doi.org/10.1016/j.fuel.2021.122599

Askarova, A., Popov, E., Ursenbach, M., Moore, G., Mehta, S. and Cheremisin, A. 2020. Experimental investigations of forward and reverse combustion for increasing oil recovery of a real oil field. *Energies*, **13**, 4581–4581, https://doi.org/10.3390/en13174581

Bjørlykke, K. 2015. *Petroleum Geoscience from Sedimentary Environments to Rock Physics*. 2nd edn. Springer Berlin Heidelberg, Berlin, Heidelberg, Germany.

Bottia-Ramirez, H., Aguillon-Macea, M., Lizcano-Rubio, H., Delgadillo-Aya, C.L. and Gadelle, C. 2017. Numerical modeling on in-situ combustion process in the Chichimene Field: ignition stage. *Journal of Petroleum Science and Engineering*, **154**, 462–468, https://doi.org/10.1016/j.petrol.2017.02.023

Burger, J.G. 1972. Chemical aspects of in-situ combustion - heat of combustion and kinetics. *Society of Petroleum Engineers Journal*, **12**, 410–422, https://doi.org/10.2118/3599-pa

Carman, P.C. 1997. Fluid flow through granular beds. *Chemical Engineering Research and Design*, **75**, S32–S48, https://doi.org/10.1016/s0263-8762(97)80003-2

Cinar, M. 2013. Creating enhanced geothermal systems in depleted oil reservoirs via in situ combustion. Thirty-Eigth Workshop on Geothermal Reservoir Enginerring, 11–13 February 2013, Stanford, California, USA. Stanford University.

CMG 2020. *STARS User Manual*. Computer Modelling Group Ltd., Calgary, Canada.

Coats, K.H. 1980. In-situ combustion model. *Society of Petroleum Engineers Journal*, **20**, 533–554, https://doi.org/10.2118/8394-pa

Cook, C.C. and Brekke, K. 2004. Productivity preservation through hydraulic propped fractures in the Eldfisk North Sea chalk field. *SPE Reservoir Evaluation & Engineering*, **7**, 105–114, https://doi.org/10.2118/88031-pa

Crookston, R.B., Culham, W.E. and Chen, W.H. 1979. A numerical simulation model for thermal recovery processes. *Society of Petroleum Engineers Journal*, **19**, 37–58, https://doi.org/10.2118/6724-pa

Department for Business, E.a.I.S. 2020. New plans to make UK world leader in green energy. Press Release.

Esmaeili, S., Sarma, H., Harding, T. and Maini, B. 2019. Correlations for effect of temperature on oil/water relative permeability in clastic reservoirs. *Fuel*, **246**, 93–103, https://doi.org/10.1016/j.fuel.2019.02.109

Fadaei, H., Castanier, L., Kamp, A.M.M., Debenest, G., Quintard, M. and Renard, G. 2011. Experimental and numerical analysis of in-situ combustion in a fractured core. *Society of Petroleum Engineers Journal*, **16**, 358–373, https://doi.org/10.2118/141117-pa

Fassihi, M.R., Meyers, K.O. and Baslle, P.F. 1990. Low-temperature oxidation of viscous crude oils. *Society of Petroleum Engineers Reservoir Engineering*, **5**, 609–616, https://doi.org/10.2118/15648-pa

Fassihi, M.R., Moore, R.G., Mehta, S.A. and Ursenbach, M.G. 2016. Safety considerations for high-pressure air injection into light-oil reservoirs and performance of the holt sand unit project. presented at the Society of Petroleum Engineers Improved Oil Recovery Symposium, 3 January 2016, Tulsa, USA.

Gluyas, J.G. and Swarbrick, R.E. 2004. *Petroleum Geoscience*. Blackwell Publishing, Malden, Massachusetts, USA.

Gutierrez, D., Moore, R.G., Mehta, S.A., Ursenbach, M.G. and Skoreyko, F. 2009. The challenge of predicting field performance of air injection projects based on laboratory and numerical modelling. *Journal of Canadian Petroleum Technology*, **48**, 23–34, https://doi.org/10.2118/09-04-23-da

Gutiérrez, D., Miller, R.J., Taylor, A.R., Thies, B.P. and Kumar, V.K. 2009. Buffalo Field high-pressure-air-injection projects: technical performance and operational challenges. *Society of Petroleum Engineers Reservoir Evaluation & Engineering*, **12**, 542–550, https://doi.org/10.2118/113254-pa

Harker, S.D. 1998. The palingenesy of the Piper oil field, UK North Sea. *Petroleum Geoscience*, **4**, 271–286, https://doi.org/10.1144/petgeo.4.3.271

Hodgins, B., Moy, D.J. and Carnicero, P.A. 2020. The Captain Field, Block 13/22a, UK North Sea. *Geological Society, London, Memoirs*, **52**, 705–716, https://doi.org/10.1144/m52-2018-92

Ito, Y. and Chow, A.K.-Y. 1988. A field scale in-situ combustion simulator with channeling considerations. *Society of Petroleum Engineers Reservoir Engineering*, **3**, 419–430, https://doi.org/10.2118/13220-pa

Ji, D., Xu, J., Lyu, X., Li, Z. and Zhan, J. 2022. Numerical modeling of the steam chamber ramp-up phase in steam-assisted gravity drainage. *Energies*, **15**, 2933, https://doi.org/10.3390/en15082933

Jia, N., Law, D.H.S., Naccache, P. and Giddins, M.A. 2016. Applicability of kinetic models for in situ combustion processes with different oil types. *Natural Resources Research*, **26**, 37–55, https://doi.org/10.1007/s11053-016-9299-y

Jolliffe, I.T. and Cadima, J. 2016. Principal component analysis: a review and recent developments. *Philosophical Transactions of the Royal Society A: Mathematical, Physical and Engineering Sciences*, **374**, 20150202, https://doi.org/10.1098/rsta.2015.0202

Joseph, C., Jay, C.B. and Eslinger, E.V. 1983. Evaluation of an in-situ combustion process by postburn core and log analysis. *Journal of Petroleum Technology*, **35**, 827–835, https://doi.org/10.2118/10766-pa

Kozeny, J. 1927. *Über kapillare Leitung des Wassers im Boden: (Aufstieg, Versickerung und Anwendung auf die Bewässerg)*. Hölder-Pichler-Tempsky, A.-G. [Abt.:] Akad. d. Wiss.

Kumar, V.K., Fassihi, M.R. and Yannimaras, D.V. 1995. Case history and appraisal of the Medicine Pole Hills unit air-injection project. *Society of Petroleum Engineers Reservoir Engineering*, **10**, 198–202, https://doi.org/10.2118/27792-pa

Li, T., Zhu, J., Xin, S. and Zhang, W. 2014. A novel geothermal system combined power generation, gathering heat tracing, heating/domestic hot water and oil recovery in an oilfield. *Geothermics*, **51**, 388–396, https://doi.org/10.1016/j.geothermics.2014.03.009

Ling, K., Shen, Z., Han, G. and He, J. 2014. A review of enhanced oil recovery methods applied in Williston Basin. presented at the Proceedings of the 2nd Unconventional Resources Technology Conference, 25–27 August 2014, Denver, Colorado, USA.

Liu, D., Tang, J., Zheng, R. and Song, Q. 2021. Determination of the propagation state of the combustion zone during in-situ combustion by dimensionless numbers. *Fuel*, **284**, https://doi.org/10.1016/j.fuel.2020.118972

Mackertich, D. 1996. The Fife Field, UK central North Sea. *Petroleum Geoscience*, **2**, 373–380, https://doi.org/10.1144/petgeo.2.4.373

Maes, J., Muggeridge, A.H., Jackson, M.D., Quintard, M. and Lapene, A. 2017. Scaling analysis of the in-situ upgrading of heavy oil and oil shale. *Fuel*, **195**, 299–313, https://doi.org/10.1016/j.fuel.2017.01.072

Moore, I., Archer, J. and Peavot, D. 2020. The Alba Field, Block 16/26a, UK North Sea. *Geological Society, London, Memoirs*, **52**, 637–650, https://doi.org/10.1144/m52-2018-46

Ng, J.T.H. and Egbogah, E.O. 1983. An improved temperature-viscosity correlation for crude oil systems. 34th Annual Technical Meeting of The Petroleum Society, 10–13 May 1983, Banff, Canada. Petroleum Society of Canada.

Olivarius, M., Weibel, R., Hjuler, M.L., Kristensen, L., Mathiesen, A., Nielsen, L.H. and Kjøller, C. 2015. Diagenetic effects on porosity–permeability relationships in red beds of the Lower Triassic Bunter Sandstone Formation in the North German Basin. *Sedimentary Geology*, **321**, 139–153, https://doi.org/10.1016/j.sedgeo.2015.03.003

Parkes, L., Wood, P. and Macdonald, C. 2020. The Kraken and Kraken North fields, Block 9/2b, UK North Sea. *Geological Society, London, Memoirs*, **52**, 863–874, https://doi.org/10.1144/m52-2018-64

Pinnock, S.J. and Clitheroe, A.R.J. 1997. The Captain Field, UK North Sea; appraisal and development of a viscous oil accumulation. *Petroleum Geoscience*, **3**, 305–312, https://doi.org/10.1144/petgeo.3.4.305

Ranjbar, M. and Pusch, G. 1991. Pyrolysis and combustion kinetics of crude oils, asphaltenes and resins in relation to thermal recovery processes. *Journal of Analytical and Applied Pyrolysis*, **20**, 185–196, https://doi.org/10.1016/0165-2370(91)80072-g

Reid, R.C., Prausnitz, J.M. and Sherwood, T.K. 1977. *The Properties of Gases and Liquids*. McGraw-Hill.

Ren, S.R., Greaves, M. and Rathbone, R.R. 2002. Air injection LTO Process: an IOR technique for light-oil reservoirs. *Society of Petroleum Engineers Journal*, **7**, 90–99, https://doi.org/10.2118/57005-pa

Robertson, A.G., Ball, M. *et al.* 2020. The Clair Field, Blocks 206/7a, 206/8, 206/9a, 206/12a and 206/13a, UK Atlantic Margin. *Geological Society, London, Memoirs*, **52**, 931–951, https://doi.org/10.1144/m52-2018-76

Rose, P.T.S., Byerley, G.W. *et al.* 2020. The Forties Field, Blocks 21/10 and 22/6a, UK North Sea. *Geological Society, London, Memoirs*, **52**, 454–467, https://doi.org/doi:10.1144/M52-2017-41

Sarathi, P.S. 1999. *In-Situ Combustion Handbook – Principles and Practices*. Office of Scientific and Technical Information (OSTI), Tulsa, Oklahoma, USA.

Schiffner, D., Kecinski, M. and Mohapatra, S. 2021. An updated look at petroleum well leaks, ineffective policies and the social cost of methane in Canada's largest oil-producing province. *Climatic Change*, **164**, https://doi.org/10.1007/s10584-021-03044-w

Sharma, J., Dean, J., Aljaberi, F. and Altememee, N. 2021. In-situ combustion in Bellevue field in Louisiana – History, current state and future strategies. *Fuel*, **284**, https://doi.org/10.1016/j.fuel.2020.118992

Shepherd, M. (ed) 2009. Chapter 5 - Factors influencing recovery from oil and gas fields. *Oil Field Production Geology. AAPG Memoir*, **9**. American Association of Petroleum Geologists, Tulsa, Oklahoma, USA, 37–46.

Silcock, S.Y., Baptie, R.J., Iheobi, A., Frost, S., Simms, A. and Brettle, M. 2020. The Mariner Field, Block 9/11a, UK North Sea. *Geological Society, London, Memoirs*, **52**, 886–896, https://doi.org/10.1144/m52-2017-44

Speight, J.G. 2019. *Heavy oil Recovery and Upgrading*. Gulf Professional Publishing, Cambridge, MA.

Standing, M.B. 1947. A pressure-volume-temperature correlation for mixtures of California oils and gases. Drilling and Production Practice.

Storey, B.M., Worden, R.H. and McNamara, D.D. 2022. The geoscience of in-situ combustion and high-pressure air injection. *Geosciences*, **12**, 340, https://doi.org/10.3390/geosciences12090340

Struna, S.M. and Poettmann, F.H. 1988. In-situ combustion in the Lower Hospah Formation, McKinley County, New Mexico. *Society of Petroleum Engineers Reservoir Engineering*, **3**, 440–448, https://doi.org/10.2118/14917-pa

Templeton, J.D., Ghoreishi-Madiseh, S.A., Hassani, F. and Al-Khawaja, M.J. 2014. Abandoned petroleum wells as sustainable sources of geothermal energy. *Energy*, **70**, 366–373, https://doi.org/10.1016/j.energy.2014.04.006

Tiab, D. and Donaldson, E.C. 2015. *Petrophysics Theory and Practice of Measuring Reservoir Rock and Fluid Transport Properties*. 4th edn. ed. Gulf Professional Pubishing, Amsterdam.

Turta, A.T., Chattopadhyay, S.K., Bhattacharya, R.N., Condrachi, A. and Hanson, W. 2007. Current status of commercial in situ combustion projects worldwide. *Journal of Canadian Petroleum Technology*, **46**, 8–14, https://doi.org/10.2118/07-11-ge

Vinsome, P.K.W. and Westerveld, J. 1980. A simple method for predicting cap and base rock heat losses in' thermal reservoir simulators. *Journal of Canadian Petroleum Technology*, **19**, 87–90, https://doi.org/10.2118/80-03-04

Watson, K., Nelson, E. and Murphy, G.B. 1935. Characterization of petroleum fractions. *Industrial & Engineering Chemistry*, **27**, 1460–1464, https://doi.org/10.1021/ie50312a018

Worden, R.H. and Utley, J.E.P. 2022. Automated mineralogy (SEM-EDS) approach to sandstone reservoir quality and diagenesis. *Frontiers in Earth Science*, **10**, https://doi.org/10.3389/feart.2022.794266

Wu, C.H. and Fulton, P.F. 1971. Experimental simulation of the zones preceding the combustion front of an in-situ combustion process. *Society of Petroleum Engineers Journal*, **11**, 38–46, https://doi.org/10.2118/2816-pa

Wynn, T. and Saundry, E. 2020. The Buchan Field, Blocks 20/5a and 21/1a, UK North Sea. *Geological Society, London, Memoirs*, **52**, 679–690, https://doi.org/10.1144/M52-2018-11

Yang, M., Harding, T.G. and Chen, Z. 2019. Field-scale modeling of hybrid steam and in-situ-combustion recovery process in oil-sands reservoirs using dynamic gridding. *Society of Petroleum Engineers Reservoir Evaluation & Engineering*, **23**, 311–325, https://doi.org/10.2118/189726-pa

Zhu, Z. 2011. Upscaling for field-scale in-situ combustion simulation. presented at the Society of Petroleum Engineers Annual Technical Conference and Exhibition, 30 October–2 November 2011, Denver, Colorado.

Zhu, Y., Li, K., Liu, C. and Mgijimi, M.B. 2019. Geothermal power production from abandoned oil reservoirs using in situ combustion technology. *Energies*, **12**, 4476–4476, https://doi.org/10.3390/en12234476

Zhu, Z., Liu, C., Chen, Y., Gong, Y., Song, Y. and Tang, J. 2021. In-situ combustion simulation from laboratory to field scale. *Geofluids*, **2021**, 1–12, https://doi.org/10.1155/2021/8153583